

Adrenal Lesions Diagnosis: Machine Learning Approach

Bernardo Gonçalves - 58885 - Doctoral program in Biomedical Engineering

January 5, 2023

1 Adrenal Glands and Lesions

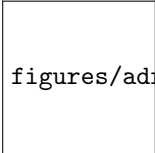
1.1 Anatomy, physiology and pathophysiology

The adrenal glands, or suprarenal glands, are two small glands located on top of the kidneys. Each has a body and two limbs **Baba2012**, and weights about 5g **brit**. Figure ?? shows the localisation and anatomy of the adrenal glands. These glands are a component of the Hypothalamic-Pituitary-Adrenal (HPA) axis, which is responsible to maintain homeostasis in the presence of chronic stressors, activating a complex range of responses from the endocrine, nervous and immune systems, generally known as the stress response **open**.

The adrenal glands can be affected by a wide variety of benign and malignant lesions. Approximately 9% of the global population is estimated to have adrenal lesions, which are mostly detected incidentally during abdominal imaging **Dhamija2015**. These lesions can be primary if they originated in the glands themselves (cortex or medulla) or secondary if they have another origin. Primary lesions can be functional if they produce hormones **Panda2015**. Table ?? presents the adrenal lesions and their classification. Adrenal adenomas represent 50-80% of adrenal lesions **Bracci2022**. Adenomas are often non-functional and remain asymptomatic, being discovered incidentally **Platzek2019**. Adrenocortical carcinomas, despite being the most common primary adrenal lesion, are very rare, presenting only 0.7–2.0 cases per million habitants per year **Bracci2022**. These lesions affect children in their first decade and adults in their fourth and fifth decades **Panda2015**. Also, the adrenals are a frequent location of metastases **Platzek2019**, approximately, 25% of patients with cancer have adrenal metastases on autopsy **Bracci2022**. In general, non-functional lesions do not require any treatment, therefore it is crucial to differentiate between adenomas and non-adenomas **Platzek2019**. Adrenal adenomas have less than 1 cm in diameter, usually and they can be lipid-rich or lipid-poor **Panda2015**. About 70-80% of the adenomas are lipid-rich in contrast with the malignant lesions **Platzek2019**. This results in a 20-30% overlap between adenomas and malignant lesions in terms of intracytoplasmic lipid content **Israel2004**.

In general, non-functional lesions do not require any treatment, therefore it is crucial to differentiate between adenomas (typical non-functional lesions) and non-adenomas **Platzek2019**. Adrenal adenomas have less than 1 cm in diameter, usually and they can be lipid-rich or lipid-poor **Panda2015**. About 70-80 % of the adenomas are lipid-rich in contrast with the malignant lesions **Platzek2019**. This results in a 20-30 % overlap between adenomas and malignant lesions in terms of intracytoplasmic lipid content **Israel2004**.

Functional lesions can cause endocrines syndromes, such as Conn and Cushing syndrome. Cushing syndrome or hypercortisolism is caused by elevated cortisol values and is associated with adrenal adenomas. However, adrenocortical carcinomas or pheochromocytomas can also cause Cushing syndrome. This syndrome is defined by symptoms such as obesity, rounded face, abnormal skin pigmentation, muscle weakness, hypertension, diabetes, and others. On the other hand, the Conn syndrome or primary aldosteronism is related to the excessive production of aldosterone. The most common symptoms of this syndrome are sodium retention, plasma renin suppression, hypertension, cardiovascular damage, and increased potassium excretion. Like the Conn syndrome, this



figures/adrenal_anatomy_cropped.png

Figure 1: Adrenal glands localisation and anatomy. Adapted from **Grossman2022**

Adrenal Lesions	Histologic origin	Benign	Malign
Primary	Cortical	Adenoma Adrenal hyperplasia Oncocytoma	Adrenocortical Carcinoma Malignant oncocytoma
	Medullary	Pheochromocytoma Ganglioneuroma	Malignant pheochromocytoma Neuroblastoma Ganglioneuroblastoma
Secondary	No specific origin	Myelolipoma Cysts Lipoma Hemorrhage	Metastases Lymphoma
Other entities	Any cell origin/ either primary or secondary	Incidentalomas Collision tumours (adenoma+myelolipoma)	Collision tumours (adenoma+metastases)

Table 1: Classification of the most common adrenal lesions in terms of their etiology and cell of origin. Adapted from **Panda2015**.

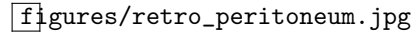


Figure 2: Peritoneum representation. Adrenals are an example of a retroperitoneal organ. From **retroimg**

syndrome is commonly caused by adrenal adenomas. In opposition to the above-mentioned syndromes, the Addison disease is caused by adrenal insufficiency, which can be caused by malignant lesions. Patients with this disease can experience weight loss, weakness, fatigue, gastrointestinal upset, orthostatic hypotension, and abnormal skin pigmentation. These symptoms can progress to dehydration, shock, hyperkalaemia (high potassium) and hyponatremia (high sodium) when entering acute adrenal insufficiency **Wang2018**.


The adrenal gland has two different regions: the adrenal cortex and the adrenal medulla. The adrenal cortex is the outer region of the gland and is derived from neural crest cells. The cortex itself comprises three zones: zona glomerosa, the zona fasciculata, and zona reticularis, each responsible for producing a different set of hormones. The adrenal cortex secretes hormones relevant to the regulation of long-term stress response, blood pressure and blood volume, nutrient uptake and storage, fluid and electrolyte balance, and inflammation. For example, this region is responsible for producing cortisol, corticosterone, and cortisone, which increase blood glucose levels, and aldosterone production, which increases the sodium level in blood **open**.

The adrenal medulla is the inner region of the gland, and it is a neuroendocrine tissue composed of postganglionic sympathetic nervous system (SNS) neurons. This region is responsible for the production of epinephrine and norepinephrine, which mediate the short-term stress or the fight-or-flight response. This response has the goal of prepare the body for extreme physical exertion **open**.

1.2 Adrenal Imaging - medical diagnosis of adrenal lesions

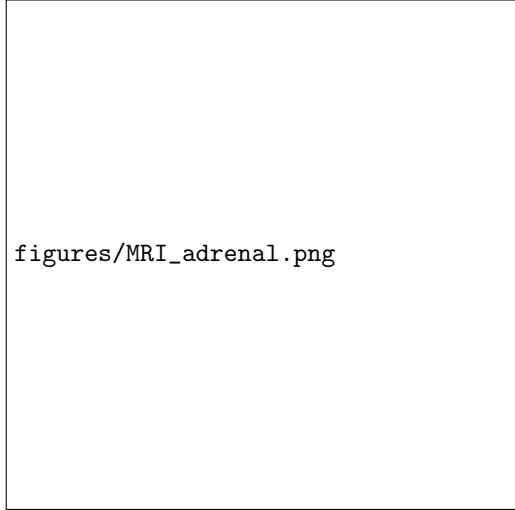
Structural medical imaging techniques are decisive in detecting and characterising adrenal lesions and complementary to functional imaging and endocrine evaluation in the assessment of functional lesions. Imaging techniques can also rule out invasive interventions. The most used imaging techniques to evaluate the adrenal glands are Computed Tomography (CT) and Magnetic Resonance Imaging (MRI). Ultrasonography (USG), although a common method to assess abdominal pathologies, is not a good method to perceive retroperitoneal structures (see Figure ??) such as adrenals **Panda2015**.

Figure ?? shows the V- (left) and Y-shaped (right) normal glands. Figure ?? is an axial contrast-enhanced CT image in the arterial phase where both glands are enhanced due to the high retroperitoneal fat content. Figure ?? is a coronal MR Chemical Shift Image (CSI) out-of-phase



figures/CT_adrenal_enhanced.png

(a) Adrenal glands in a contrast-enhanced CT axial slice in arterial phase. Due to the high level of retroperitoneal fat both glands are enhanced in this image slice. Reprinted from **Panda2015**.



figures/MRI_adrenal.png

(b) Adrenal glands in a MR CSI coronal slice. Both glands have a intermediate signal intensity. Reprinted from **Panda2015**.

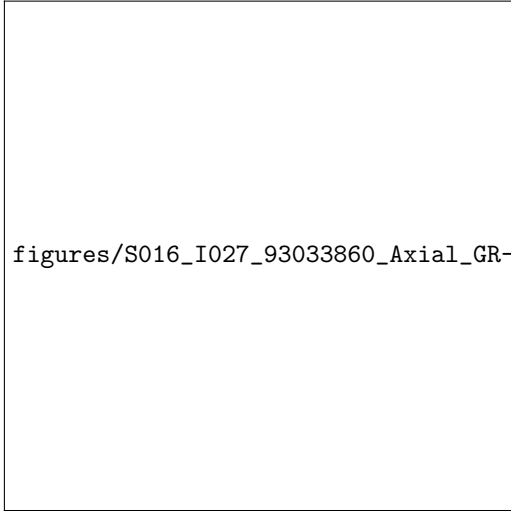
Figure 3: Normal adrenal glands in CT and MR slices. The arrows indicate the localization of the glands.

showing normal adrenal glands as well.

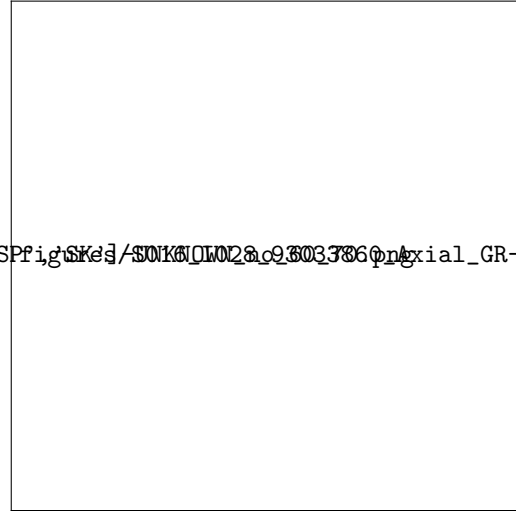
As stated above, the differential diagnosis between adenomas and non-adenomas is of extreme importance. This diagnosis can be hindered by the existence of lipid-poor adenomas that are more difficult to diagnose. Lipid-rich adenomas can be easily detected using unenhanced CT (less than 10 HU) **Panda2015** or CSI **Platzek2019**. However, unenhanced CT is not indicated to detect lipid-poor adenomas **Israel2004**. In these cases, CSI presents itself as a better solution because of its improved sensitivity to low levels of lipid content and therefore it can detect 62-67% of the adenomas uncharacterized by unenhanced CT **Israel2004**.

CSI is a fat-suppression technique that originates two sets of images: in-phase (IP) and out-of-phase (OP) images. In OP images the signal is the difference between the signals of water and fat molecules. In IP images the signal of both water and fat is added. Thus, there is a significant suppression of the signal from IP to OP images in lipid-rich lesions **Jahanvi2021**. OP images are characterised by the so-called India ink artefact, which is a signal void in the margins of fatty and normal tissues **Jahanvi2021**, creating a darker boundary in lipid-rich lesions such as most adenomas. Figure ?? shows two adenomas, one lipid-rich (up) and the other lipid-poor (down) using CSI. The red rectangles present in the figures surround the adenomas. Here, the difference in signal between IP and OP images is much greater in lipid-rich adenomas than in lipid-poor adenomas, facilitating the diagnostic process of lipid-rich adenomas using these images. Given these images, the diagnosis of adenoma can be made by visual evaluation or by quantitative indices such as the adrenal Signal Intensity Index (SII), Adrenal-to-Spleen Ratio (ASR), Adrenal-to-Liver Ratio (ALR) or the Adrenal-to-Muscle Ratio (AMR) **Fujiyoshi2003**. **Platzek2019** performed a metanalysis with 1280 lesions (859 adenomas, 421 non-adenomas) and documented a sensitivity of 94% and a specificity of 95% in detecting adrenal adenomas with the CSI technique using visual evaluation and/or quantitative methods. Despite these high values the authors state that the lipid-poor adenoma poses an issue even using CSI methods.

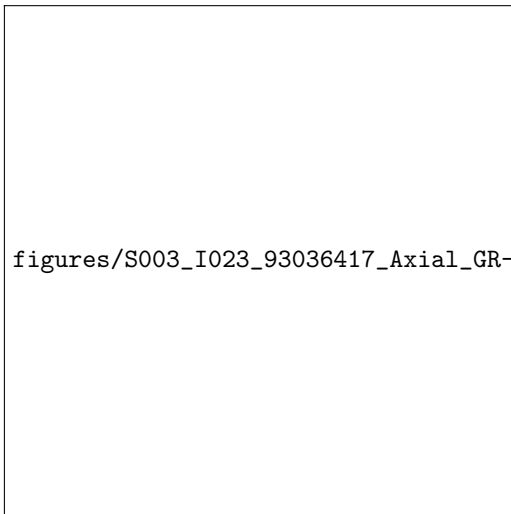
In these cases the addition of Dynamic Contrast-Enhanced (DCE) sequences is favourable, increasing the diagnosis performance **Barat2022**. In **Chung2001** 35 adrenal adenomas were analysed and it was concluded that the enhancement pattern of the adenomas is different from the one presented by malignant lesions. Adenomas present a homogeneous capillary blush on 18 seconds post-gadolinium images and a rapid washout on 45 seconds post-gadolinium images. From metanalysis performed in **Platzek2019** it was concluded that the quantitative methods do not present a significant advantage to the visual diagnosis. In addition, the authors do not recommend any additional imaging if the adenoma diagnosis is confirmed based on CSI. However, if the adenoma is not confirmed, DCE sequences would help distinguish between adenomas and malignant lesions.



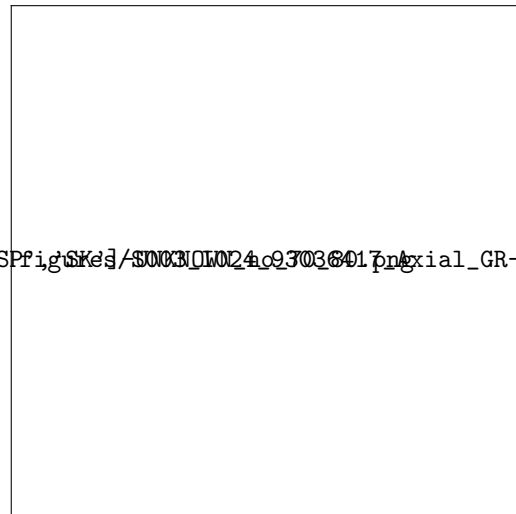
(a) T1-weighted out-of-phase axial slice with a lipid-rich adenoma.



(b) T1-weighted in-phase axial slice with a lipid-rich adenoma.



(c) T1-weighted out-of-phase axial slice with a lipid-poor adenoma.



(d) T1-weighted in-phase axial slice with a lipid-poor adenoma.

Figure 4: Adrenal adenomas in axial MR CSI. The red rectangles surround the adenomas. Lipid-rich adenomas have a much greater intensity difference between in-phase and out-of-phase images.

2 Diagnosis of adrenal lesions - a machine learning approach

The growing number of abdominal studies reflects on the increasing frequency of adrenal incidentalomas, which are usually benign, non-functional adenomas. However, it is important to evaluate their functional status and potential for being malignant as soon as possible. The diagnosis of adrenal lesions is a complex process that involves both biochemical and radiological evaluation **Anagnostis2009**. Adrenal radiologic evaluation via conventional imaging is a challenging process that depends largely on the experience and knowledge of the radiologist **Zhang2022**. Several pitfalls can result in misdiagnosis of adrenal lesions, such as the presence of pseudolesions, overlap of imaging features of different lesions, or incorrect choice of the imaging technique **Elsayes2020**. New approaches to the diagnosis of adrenal lesions are crucial to avoid misdiagnosis, which can lead to increased treatment costs or unnecessary examination **Zhang2022**. Machine learning methods have been proposed as a potential solution not only to improve the diagnostic accuracy of adrenal lesions, but also to simplify and speed up the process. These methods have proven their value in medical imaging analysis with promising results in different anatomic regions **Suganyadevi2022**, **Avanzo2020**. In this section it was conducted a thorough analysis of the published studies that perform adrenal lesion diagnosis using machine learning methods for medical imaging analysis.

2.1 Research details

The studies analysed in this section were selected accordingly in the following PICO criteria:

P (patients) – patients with adrenal lesions.

I (interventions) – machine learning (including deep learning) modelling.

C (comparison) – standard of care imaging including Computed Tomography (CT) and Magnetic Imaging Resonance (MRI).

O (outcome) – lesion differentiation (benign/malign and subtyping) and lesions detection.

The studies were searched in two databases: PubMed and Web of Science in September 2022. The search was made with the following research string: (adrenal or suprarenal) AND (CT OR "computed tomography" OR MRI OR "magnetic resonance imaging" OR "MRI scan" OR "nuclear magnetic resonance" OR "magnetic resonance" OR NMR) AND ("deep learning" OR "convolutional networks" OR CNN OR "neural networks" OR convolutional OR DNN OR SVM OR "Support vector machine" OR "decision tree" OR "machine learning"). Studies that were: (a) reviews, (b) not written in English, (c) did not report a modelling method, (d) did not have the full text available were excluded from this research.

The research resulted in 23 studies that were divided in 3 groups related with their object of study:

Group A: contains all the studies that focus on the differentiation between adrenal adenomas and other adrenal lesions.

Group B: contains all the studies that target the differentiation between benign and malignant adrenal lesions.

Group C: contains the remaining studies that did not fit any of the above categories.

Table ?? shows the distribution of the selected studies in terms of their group, image modality and model type. Overall, most of the studies adopt traditional machine learning models to classify imaging features (radiomics) from CT images to distinguish adenomas from other types of adrenal lesions, eg. Metastases, pheochromocytomas.

2.2 Radiomics

Radiomics is the extraction of quantitative features from medical images. Before the feature extraction, there are two relevant steps: image acquisition and segmentation of the region of interest (ROI). Any type of medical images can be used in radiomics, such as Positron Emission Tomography (PET), MRI, or CT. The ROI segmentation is necessary to limit the amount of data that needs to be processed in order to extract features. This process can be completely manual, which is the gold standard, where a specialist selects the ROI. Manual segmentation is a time-consuming task that significantly depends on the skill of the operator. There are fully

Group	Image Modality			Model Type			Total
	MRI	CT	MRI+CT	ML	DL	ML+DL	
A - Adenomas vs other lesions	4	7	1	11	1	0	12
B - Benign vs Malign	2	5	0	7	0	0	7
C - Other	1	3	0	2	1	1	4
Sum	7	15	1	20	2	1	23

Table 2: Studies distribution per group. CT: Computed Tomography; MRI: Magnetic Resonance Imaging; ML: Traditional Machine Learning; DL: Deep Learning.

automatic methods for ROI segmentation however, they can fail in difficult cases, such as, lesions with indistinct borders and are highly dependent on the quality of the image. For that reason, the usage of semi-automatic methods is preferable. These methods have minimal user interaction (seed identification or manual correction). The extracted quantitative features aim to describe the complexity of the individual region of interest. Ordinarily, these features are divided into 4 categories:

1. Shape-Based Features: numeric information respecting geometrics characteristics, like shape and size.
2. First-Order Statistics: distribution of voxel values without spatial information, generally histogram-based.
3. Second-Order Statistics: “texture” features, focus on the spatial relationships between voxels with similar grey levels.
4. High-Order Statistics: usage of filters to extract patterns from the images. From the resultant images, first and second-order features are extracted.

The most relevant radiomic features to the task in hand are selected using statistical approaches or machine learning **Zhang2022**. Then, these features are used as the input of ML models to classify the region of interest. This type of workflow is widespread, appearing in 87% (20/23) of the analysed studies. Traditional machine learning models like K-means, Support Vector Machine (SVM), Logistic Regression (LogReg), or Random Forest (RanFor), are frequently used to classify radiomic features of regions of interest and have achieved high performance in different anatomical regions **Zhang2022**, **Wagner2021**. Deep Learning models, such as, Convolutional Neural Networks (CNNs), have been often applied to medical images from several anatomical regions with promising results **Anaya-Isaza2021**. Despite that, only 13% of the studies presented in this paper report the application of DL models to adrenal images. DL models are different from ML models mostly because they demand bigger annotated data sets and they do not rely on the feature extraction step (all features are automatically extracted and classified by the model).

In the next 3 sections each group of papers will be analysed in detail, exploring their common and contrasting aspects. For each group, the analysis will be In the next sections each group of papers will be analysed in detail, exploring focused on the utilized data sets, models, and the obtained results.

2.3 Study Analysis

2.3.1 Group A - Adenomas vs other lesions

Group A comprises all studies that focus on the differentiation between adenomas and other lesions. This group corresponds to 52% of all analysed studies. Tables ??, ?? and ?? present an overview of the data sets, models, and results, respectively, for each study within group A.

Adenomas are the common lesion in all of these studies however they are compared with three different lesions: metastases in **Schieda2017**, **Tu2018**, **Tu2020**; pheochromocytomas in **Yi20181**, **Yi2018**, **Liu2022**, **Liu2021**, and carcinomas in **Elmohr2019**, **Torresan2021**, **Ho2019**. **Tu2020**, **Yi2018**, **Yi20181**, **Liu2022** have considered only lipid-poor adenomas for their adenoma dataset. There is only one study that has a non-binary data set. **Romeo2018** data set has 3 classes: lipid-poor adenomas, lipid-rich adenomas and non-adenomas. **Kusunoki2022** does not specify another lesion type, performing differentiation between adenomas and non-adenomas. Most of the data sets (8 of 12 studies) contain CT images. From those, 6 use both images with and

Reference	Image Modality	Sample Size (lesions)		
		Total	Adenomas	Other
Tu2018	U-CT	76	36	40
Yi20181	U/CE-CT	110	80	30
Yi2018	U-CT	265	181	84
Elmohr2019	CE-CT	54	25	29
Torresan2021	U/CE-CT	19	9	10
Kusunoki2022	U/CE-CT	115	83	32
Liu2022	U/CE-CT	280	188	92
Ho2019	U/CE-CT; T1W-OP/IP MRI	23	15	8
Liu2021	T1W-OP/IP; T2W MRI	60	40	20
Schieda2017	T1W-OP/IP; T2W MRI	44	29	15
Tu2020	T1W-OP/IP; T2W MRI	63	23	40
Romeo2018	T1W-OP/IP; T2W MRI	60	40	20

Table 3: Dataset Details for each article in the Group A. CT: Computed Tomography; U: Un-enhanced; CE: Contrast Enhanced; MRI: Magnetic Resonance Imaging; OP: Out-of-phase; IP: In-phase; T1W: T1-weighted; T2W: T2-weighted.

without contrast. The remaining have MRI datasets, all with CSI and T2W images. The sample size of the studies ranges from dozens to hundreds of lesions, which is closely related to the applied inclusion criteria and the initial sample size. For example, **Torresan2021** had a database of 336 patients however only 19 met the inclusion criteria, each with one lesion. Many of the studies have unbalance datasets. Many of the datasets have more adenomas than other lesions.

All studies, except one, performed lesion classification with ML models using radiomic features. The most frequent model is logistic regression (LogReg), followed by the support vector machine (SVM) and decision tree-based models. In every study, the region of interest (ROI) was manually selected by experts. The extraction of first and second-order statistics is a widespread practice, but only 3 studies extracted shape-based features, and none extracted higher-order statistics. The only study that has implemented a DL model has performed ROI (selected, cropped and labelled by experts) classification with a deep convolution neural network **Kusunoki2022**. They report the usage of augmentation techniques such as rotations and horizontal flips. **Torresan2021** was the only study to implement an unsupervised model.

In **Ho2019** the data set consists of lipid-poor adenomas and carcinomas in both MRI and CT images. The objective of this work was to compare the different image modalities using the same machine learning approach. The authors have reported only the Area Under the Receiving Operating Characteristic Curve (AUC). The value presented in ?? refers to the best result, using CE-CT images and with MRI images the value decreases to 58 %.

Both works by Yi et al **Yi2018**, **Yi20181** implemented a logistic regression model with the same radiomic features but using different CT images and achieved impressive results. However, **Yi2018** adds clinical features such as necrosis or calcification and lesion dimensions, to the radiomic features. Also, to improve feature selection the authors used the Least Absolute Shrinkage and Selection Operator (LASSO). However, **Yi2018** adds clinical features such as necrosis or calcification and lesion dimensions, to the radiomic features. Also, to improve feature selection the authors used the Least Absolute Shrinkage and Selection Operator (LASSO). These studies achieved the best results of this group. However, in terms of sensitivity, **Yi2018** has achieved an higher value. Overall, there are 4 studies in which their metrics average more than 90%: **Yi2018**, **Yi20181**, **Kusunoki2022**, **Schieda2017**. Three of them use CT images. **Schieda2017** had a very small unbalanced dataset and used CSI images.

2.3.2 Group B - Malign vs benign lesions

Group B consists of studies that aim at the differentiation between benign and malignant lesions. This group includes 30??, ?? and ?? display an overview of the data sets, models, and results, respectively, for each study within group B.

In terms of the image modalities in the data sets, this group is similar to group A. There are more studies that use CT images and all of them, except one, use CE-CT. Studies that analyse MRI data sets have both T1W chemical shift images and T2W images. The number of lesions analysed in each study varies from dozens to hundreds like in group A and most data sets are

Reference	Type	Classification Model	ROI	Features
Tu2018	ML	LogReg	Manual	1 st
Yi20181	ML	LogReg	Manual	1 st , 2 nd , higher
Yi2018	ML	LogReg	Manual	1 st , 2 nd , higher
Elmohr2019	ML	RanFor; LogReg	Manual	1 st , 2 nd , shape
Torresan2021	ML	K-Means	Manual	1 st , 2 nd
Kusunoki2022	DL	DCNN	Manual	-
Liu2022	ML	LinReg; SVM; RanFor	Manual	1 st ; clinical
Ho2019	ML	LogReg	Manual	1 st , 2 nd , shape
Liu2021	ML	SVM	Manual	1 st
Schieda2017	ML	LogReg	Manual	1 st
Tu2020	ML	LogReg	Manual	1 st , shape
Romeo2018	ML	DecTre	Manual	1 st , 2 nd

Table 4: Modelling Details for each article in the Group A. ML: Traditional Machine Learning models; DL: Deep Learning models; LogReg: Logistic Regression; LASSO: Least Absolute Shrinkage and Selection Operator; DecTre: Decision Tree; RanFor: Random Forest; PCA: Principal Components Analysis; SVM: Support Vector Machine; 1st, 2nd, higher: first, second, higher order statistics, respectively; shape: shape-based features.

Reference	Specificity - %	Sensitivity - %	Accuracy - %	AUC - %
Tu2018	75.0	47.5	60.5	65.0
Yi20181	97.5	86.2	94.4	95.2
Yi2018	90.3	95.5	92.0	95.7
Elmohr2019	83.0	81.0	82.0	89.0
Torresan2021	90.0	87.5	88.9	-
Kusunoki2022	96.0	87.0	94.0	-
Liu2022	86.6	89.2	87.5	-
Ho2019	-	-	80.0	-
Liu2021	-	-	85.0	91.7
Schieda2017	86.2	93.3	88.6	97.0
Tu2020	100	75.0	84.1	-
Romeo2018	-	-	80.0	-

Table 5: Model metrics for each article in the Group A. AUC: Area Under the Receiving Operating Characteristic Curve.

Reference	Image Modality	Sample Size (lesions)		
		Total	Benign	Malign
Shoemaker2018	U-CT	377	182	195
Koyuncu2019	CE-CT	114	90	24
Li2019	U/CE-CT	210	114	96
Andersen2021	CE-CT	160	89	71
Moawad2021	U/CE-CT	40	21	19
Barstugan2020	T1W-OP/IP; T2W MRI	122	112	10
Stanzione2021	T1W-OP/IP; T2W MRI	55	37	18

Table 6: Dataset Details for each article in the Group B. CT: Computed Tomography; U: Un-enhanced; CE: Contrast Enhanced; MRI: Magnetic Resonance Imaging; OP: Out-of-phase; IP: In-phase; T1W: T1-weighted; T2W: T2-weighted.

Reference	Type	Classification Model	ROI	Features
Shoemaker2018	ML	LogReg	-	1^{st} , 2^{nd}
Koyuncu2019	ML	NN	Semi-auto	1^{st} , 2^{nd} , higher, shape
Li2019	ML	BayCla	Semi-auto	2^{nd}
Andersen2021	ML	LogReg	Semi-auto	1^{st} , higher
Moawad2021	ML	RanFor	Manual	1^{st} , 2^{nd} , higher, shape
Barstugan2020	ML	SVM	Manual; Semi-auto	2^{nd} , higher
Stanzione2021	ML	ExTre	Manual	1^{st} , 2^{nd} , higher, shape

Table 7: Modelling Details for each article in the Group B. ML: Traditional Machine Learning models; DL: Deep Learning models; LogReg: Logistic Regression; BayCla: Bayesian Classifier; NN: Neural Network; ExTre: Extra Trees Classifier. RanFor: Random Forest; SVM: Support Vector Machine; 1^{st} , 2^{nd} , higher: first, second, higher order statistics, respectively; shape: shape-based features.

unbalanced. **Shoemaker2018** has the largest data set of all the analysed studies of all groups.

Unlike group A, most of the studies in group B implement semi-automatic region of interest segmentation. All studies except **Li2019** combine different radiomic features. In **Li2019** only second-order statistics are used as input of a Bayesian Spatial Gaussian Classifier. Group B does not include any study with a DL model, however, there are two studies that use neural networks. **Koyuncu2019** experimented several optimisation algorithms for neural networks and achieved the best results using the Bounded Particle Swarm Optimisation algorithm ¹. In **Barstugan2020** an SVM was implemented to perform binary classification, however, the authors also used a NN to perform type characterisation. The authors divided the dataset into 4 classes, each with one type of lesion, 3 benign (adenoma, cyst and lipoma) and 1 malignant (metastasis). For both workflows, ROI selection was made using manual and semi-automatic segmentation, and the same radiomic features were used. The results presented in Table ?? refer to the binary classification using manual segmentation (the results using semiautomatic segmentation were worse), , and they were the best results of this group. For the multiclass classification, the results were poor, despite the high values of specificity and accuracy, 96.2 % and 93.2 %, respectively, the sensibility is extremely low, 59.6 %, which can be explained by the high number of classes and the lack of balance in the data set. In this group, all the models are supervised learning models.

2.3.3 Group C

Group C consists of the remaining studies that did not fit any of prior defined groups. This group includes 18% of the studies. Tables ??, ?? and ?? display an overview of the data sets, models, and results, respectively, for each study inside group C.

In this group are 4 studies with distinct goals. **Bi2017** implements a fully convolutional neural network for lesion detection using a small data set of U-CT images. The network receives as input complete CT images and outputs the lesion probability map. To surpass the small data set issue, the authors applied traditional augmentation methods such as random crops and contrast

¹https://link.springer.com/chapter/10.1007/978-3-319-93025-1_2

Reference	Specificity - %	Sensitivity - %	Accuracy - %	AUC - %
Shoemaker2018	-	-	-	78.0
Koyuncu2019	82.2	75.0	80.7	78.6
Li2019	67.5	94.8	80.0	-
Andersen2021	77.0	58.0	68.0	73.0
Moawad2021	71.4	84.2	77.5	85.1
Barstugan2020	90.0	99.2	98.4	-
Stanzione2021	-	-	91.0	97.0

Table 8: Model metrics for each article in the Group B. AUC: Area Under the Receiving Operating Characteristic Curve.

Reference	Image Modality	Sample size	Task
Bi2017	U-CT	38	Lesion Detection
Bi2022	CE-CT	229	Multiclass Classification
Kong2022	T2W-MRI	305	pheo vs non-pheo
Zheng2020	U/CE-CT	83	Adenoma subtyping

Table 9: Dataset Details for each article in the Group C. CT: Computed Tomography; U: Un-enhanced; CE: Contrast Enhanced; MRI: Magnetic Resonance Imaging; OP: Out-of-phase; IP: In-phase; T1W: T1-weighted; T2W: T2-weighted. Pheo: pheochromocytomas

variations and used a pre-trained network. The lesion probability map was then refined using a random walk-based algorithm.

Bi2022 creates a machine learning pipeline where the CNN embedding is used as input of an SVM to execute multiclass classification with a data set of CE-CT images. The data set has 5 classes: carcinoma, non-functional adenoma, ganglioneuroma, myelolipoma and pheochromocytoma. A ResNet-101 pretrained in the ImageNet data set was used to create the feature embedding. To improve the toleration to intra-class variations the authors created a similarity feature learning module. Another relevant contribution was the usage of two DL networks each using a different CT image but with a weighted sharing strategy. The goal was to improve performance with a highly unbalanced data set.

Kong2022 aimed at the differentiation between pheochromocytomas and non-pheochromocytomas with a T2W MRI dataset and a logistic regression model. The presented sample size includes an external and an internal data set. The external data set was used for external validation of the developed pipeline. **Zheng2020** also used logistic regression but to characterize adenomas with a CT dataset.

2.4 Discussion

1. most promissing
2. general limitations and future developments

Reference	Type	Model	ROI	Features
Bi2017	DL	FCN	Manual	-
Bi2022	DL + ML	CNN + SVM	Manual	CNN embedding
Kong2022	ML	LogReg	Semi-Auto	1 st , 2 nd , higher, shape
Zheng2020	ML	LogReg	Manual	1 st , higher, shape

Table 10: Modelling Details for each article in the Group C. ML: Traditional Machine Learning models; DL: Deep Learning models; LogReg: Logistic Regression; BSGC: Bayesian Spatial Gaussian Classifiers; CNN: Convolutional Neural Network; SVM: Support Vector Machine; 1st, 2nd, higher: first, second, higher order statistics, respectively; shape: shape-based features.

Reference	Specificity - %	Sensitivity - %	Accuracy - %	AUC - %
Bi2017	-	76.29	-	-
Bi2022	95.9	83.7	85.2	-
Kong2022	75.0	85.7	84.0	90.6
Zheng2020	92.8	91.5	92.2	90.2

Table 11: Model metrics for each article in the Group C. AUC: Area Under the Receiving Operating Characteristic Curve.